# CO 2 -Undersaturated Melt Inclusions From the South West Indian Ridge Record Surprisingly Uniform Redox Conditions

Yves Moussallam, Guillaume Georgeais, Estelle F. Rose-Koga, Kenneth T. Koga, Margaret E Hartley, Bruno Scaillet, Clive Oppenheimer, Nial Peters

Geochemistry, Geophysics, Geosystems®

AGU ADVANCING EARTH AND SPACE SCIENCES

RESEARCH ARTICLE
10.1029/2023GC011235

# $CO_2$-Undersaturated Melt Inclusions From the South West Indian Ridge Record Surprisingly Uniform Redox Conditions

**Yves Moussallam[1,2], Guillaume Georgeais[1], Estelle F. Rose-Koga[3], Kenneth T. Koga[3], Margaret E. Hartley[4], Bruno Scaillet[3], Clive Oppenheimer[5], and Nial Peters[6]**

[1]Lamont-Doherty Earth Observatory, Columbia University, Palisades, NY, USA, [2]Department of Earth and Planetary Sciences, American Museum of Natural History, New York, NY, USA, [3]ISTO, UMR 7327, Université d'Orléans-CNRS-BRGM, Orleans, France, [4]Department of Earth and Environmental Sciences, University of Manchester, Manchester, UK, [5]Department of Geography, University of Cambridge, Cambridge, UK, [6]Department of Electronic and Electrical Engineering, University College London, London, UK

**Key Points:**

- Discovery and characterization of a new suite of $CO_2$-undersaturated melt inclusions
- High $CO_2$/CITE ratio suggests a $CO_2$-rich mantle domain
- No relation between degree of partial melting and $Fe^{3+}/\Sigma Fe$ indicates efficient buffering or decreasing $Fe_2O_3$ partition coefficient with T

**Supporting Information:**

Supporting Information may be found in the online version of this article.

**Correspondence to:**

Y. Moussallam,
yves.moussallam@ldeo.columbia.edu

**Citation:**

Moussallam, Y., Georgeais, G., Rose-Koga, E. F., Koga, K. T., Hartley, M. E., Scaillet, B., et al. (2023). $CO_2$-undersaturated melt inclusions from the South West Indian Ridge record surprisingly uniform redox conditions. *Geochemistry, Geophysics, Geosystems*, *24*, e2023GC011235. https://doi.org/10.1029/2023GC011235

Received 14 SEP 2023
Accepted 25 NOV 2023



**Abstract** The behavior of $Fe^{3+}$ during mantle partial melting strongly influences the oxidation state of the resulting magmas, with implications for the evolution of the atmosphere's oxidation state. Here, we challenge a prevailing view that low-degree partial melts are more oxidized due to the incompatible behavior of $Fe^{3+}$. Our study is based on measurements of $Fe^{3+}/\sum Fe$ along with major, minor, trace and volatile elements in olivine- and plagioclase-hosted melt inclusions of $CO_2$ undersaturated mantle melts in South West Indian Ridge lava. These inclusions record minimum entrapment pressures equivalent to depths up to 10 km below the seafloor, record magma ascent rates of 0.03–0.19 m/s, and display exceptionally high $CO_2$/Ba, $CO_2$/Rb, and $CO_2$/Nb ratios, indicative of a $CO_2$-rich mantle source. Accounting for fractional crystallization, we find a uniform melt oxidation state (with an $Fe^{3+}/\Sigma Fe$ at $0.140 \pm 0.005$ at MgO = 10 wt.%) that displays no systematic variation with major, minor, volatile or trace element contents, thus providing no evidence for a relationship between the degree of partial melting and $Fe^{3+}/\Sigma Fe$. This can be explained by efficient buffering of $Fe^{3+}/\sum Fe$ and $fO_2$ of mid-ocean ridge basalt melts by their surrounding mantle and/or a decrease in the bulk peridotite-melt $Fe_2O_3$ partition coefficient with increasing partial melting. We conclude that changes in the Earth's upper mantle temperature over geological time need not have affected the oxidation state of volcanic products or of the atmosphere.

## 1. Introduction

Nearly all mid-ocean ridge basalts (MORBs) are believed to be saturated with a $CO_2$ fluid phase during ascent and emplacement, as the $CO_2$ contents of MORB glasses typically yield volatile saturation pressures consistent with or slightly higher than their collection/eruption pressure (e.g., Aubaud, 2022; Dixon et al., 1988; Le Voyer et al., 2019; Michael & Graham, 2015; Shimizu et al., 2016, 2019). Yet, once thought to be extremely rare, occurrences of undegassed MORBs have now been documented at several locations, including:

1. The mid-Atlantic ridge, 14°N, the so-called "popping rock" (e.g., Cartigny et al., 2008; Javoy & Pineau, 1991),
2. The East Pacific Rise, 8°N, in olivine-hosted melt inclusions (MI) from the Siqueiros transform fault (Saal et al., 2002),
3. The equatorial Mid-Atlantic Ridge, 5°S, in olivine-hosted MIs (Le Voyer et al., 2017),
4. In MORB glasses with ultra-low volatile contents from the Atlantic, Pacific, Indian Ocean and Gakkel Ridge (Michael & Graham, 2015).

Here we report a new occurrence of $CO_2$-undersaturated MORBs in a suite of olivine- and plagioclase-hosted MIs and embayments collected from the South West Indian Ridge (SWIR). We present $Fe^{3+}/\Sigma Fe$ measurements obtained by means of X-ray absorption near-edge structure (XANES) spectroscopy at the iron K-edge, together with volatile, major, minor and trace element concentrations and water diffusion profiles in embayments. We show that the oxidation state of these melts, at least some of which must have been entrapped at mantle depth (minimum volatile saturation pressures of 316 MPa), is uniform, and is uncorrelated with trace element enrichment.

## 2. Samples and Methods

### 2.1. Geological Setting, Sample Description and Processing

The sample investigated for this study, EDUL_DR75_1_04 (CNRS 000 000 2592), was collected from the South West Indian Ridge (SWIR) by dredging during the EDUL (Echantillonnage d'une Dorsal Ultra Lente) campaign under the auspices of IPGP in 1997. The South West Indian Ridge (SWIR) is one of the slowest-spreading mid-ocean ridges (spreading rate ≤18 mm/year; Dick et al., 2003). It is characterized by a high isotopic heterogeneity (e.g., Hamelin & Allègre, 1985; Janney et al., 2005; Mahoney et al., 1992) and low magma supply (e.g., Cannat et al., 1999). The pillow basalt sample was collected at a depth of 2,650–2,900 m at 37°51′48″S, 49°20′12″E (https://lithotheque.ipgp.fr/edul.html), corresponding to ridge segment 28 to 29 (numbering from Cannat et al., 1999). This ridge segment has been studied by Wang et al. (2021) who suggested that the mantle source in this region is a refractory mantle residue that previously melted within a subduction zone, and is more depleted in highly incompatible trace elements relative to other regions of the SWIR. Samples from the same dredge (at 49°E; EDUL_DR75) were previously studied by Font et al. (2007). They analyzed plagioclase- and olivine-hosted MIs and concluded that they represented batches of melt generated by higher degrees of melting at greater mean depths in the mantle melting column compared with MIs from the NE end of the ridge (64°E). Font et al. (2007) also found systematic differences between plagioclase- and olivine-hosted MIs in EDUL_DR75, which they attributed to a two-step formation (see their Figure 10), with plagioclase-hosted MIs representing final batches of melt generated at the top of the mantle melting column, and olivine-hosted MIs corresponding to melts generated from less depleted, more fertile mantle at greater depths.

Sample EDUL_DR75_1_04 is porphyritic with centimeter-scale plagioclase and millimetric to sub-millimetric clinopyroxene and olivine phenocrysts within an aphyric matrix. Pillow rims are vitreous with a phenocryst proportion close to 50%. The outer 3 cm of pillow basalt samples (i.e., the rim that quenched the fastest) were sliced using a diamond saw, then ground and sieved, and crystals and glass separated magnetically. MI-bearing olivine macrocrystals in the 0.5–2 mm size fraction were hand-picked under a binocular microscope. MIs were first exposed by polishing single crystals to 0.25 µm using silicon carbide paper followed by corundum mats. We avoided using diamond polishing pastes to avoid contaminating MI surfaces with carbon. Polished crystals were subsequently mounted in indium for analysis by secondary ion mass spectrometry (SIMS) followed by electron probe microanalysis (EPMA). MIs are entirely glassy, and 25% of them contain a bubble occupying 0.3%–2% of the MI by volume (calculated from 2D observations and assuming spherical MIs and bubbles). The MIs are 58–442 µm along their long axis (average of 151 ± 67 µm). After SIMS and EPMA analyses, host olivine crystals were removed from the indium mount and polished on the reverse side, parallel to the first polish, to obtain double-polished wafers. Double-polished MIs were then mounted on a glass slide using CrystalBond for XANES analysis such that the newly exposed MI surface faced outwards. Finally, MIs were analyzed for trace elements by LA-ICP-MS.

### 2.2. Electron Probe Microanalyses (EPMA)

The major element compositions of matrix glasses, MIs and their host crystals were measured with a Cameca SX100 electron microprobe at the Laboratoire Magmas et Volcans in Clermont-Ferrand. For crystalline phases (olivine and plagioclase), beam conditions of 15 kV and 20 nA were employed, with 20 s counting times (and 20 s off peak counting times). Errors (two standard deviations) are ±0.5 for $SiO_2$, ±0.06 for $TiO_2$, ±0.04 for $Al_2O_3$, ±0.4 for FeO, ±0.07 for MnO, ±0.06 for CaO, ±0.5 for MgO, and ±0.07 for NiO. For glass analyses, the beam current was decreased to 8 nA and the beam defocused to 10 µm. Sodium was analyzed first to limit the effects of Na loss. Counting times of 10 s minimum were used (with off peak counting times similar to on peak ones). Errors (two standard deviation) are ±0.1 for $SiO_2$, ±0.07 for $Na_2O$, ±0.07 for $K_2O$, ±0.05 for $Al_2O_3$, ±0.1 for CaO, ±0.2 for FeO, ±0.1 for MgO, ±0.04 for $TiO_2$, ±0.04 for MnO, and ±0.03 for $P_2O_5$. The instrument was calibrated on natural and synthetic mineral standards and glasses: wollastonite (Si, Ca), $MnTiO_3$ (Ti, Mn), orthoclase (K and Al in minerals), standard glass VG2 (Al in glasses, see Óladóttir et al., 2008), $Cr_2O_3$ (Cr), fayalite (Fe), forsterite (Mg), NiO (Ni), albite (Na) and apatite (P).

### 2.3. Assessment of Post-Entrapment Crystallization

The amount of post-entrapment crystallization (PEC) for olivine-hosted inclusions was calculated using Petrolog3 (Danyushevsky & Plechov, 2011). Calculations were performed using the olivine-melt model

of Danyushevsky (2001), the density model of Lange and Carmichael (1987), the model for melting oxidation of Kress and Carmichael (1988) and the model of Toplis (2005) for the compositional dependence of the olivine-liquid Fe-Mg exchange coefficient (Kd). Calculations were performed assuming an oxygen-buffered system at quartz-fayalite-magnetite (QFM). The resulting PEC estimates ranged from −11% to 0.3%, with an average of −3% and standard deviation of ±2%. Performing the same calculations assuming a closed system to $fO_2$ yields similar results with a range from −8 to 1%, an average of −1% and standard deviation of ±2%. Given these results and the fact that calculations in Petrolog3 are performed assuming anhydrous conditions at 1 atm (i.e., conditions that are far from natural ones), we did not modify the MI compositions from their measured values.

### 2.4. Secondary Ion Mass Spectrometry (SIMS)

Volatile ($H_2O$, $CO_2$, Cl, F, S) contents in MIs, embayments and matrix glasses were determined using a Cameca IMS 1280 multi-collection ion microprobe at CRPG-CNRS-Nancy during the same analytical session and hence the same analytical conditions as reported in Moussallam et al. (2021). We used a $Cs^+$ primary beam with a current of 1 nA and an electron gun to compensate for the charge build-up at the sample surface. A 3-min pre-sputter with a 30 μm × 30 μm square raster was applied, and then analyses were performed on the 15–20 μm spot in the center of the clean rastered area using a mechanical aperture placed at the secondary ion image plane. We collected signals for $^{12}C$ (8 s), $^{17}O$ (3 s), $^{16}O^1H$ (6 s), $^{18}O$ (3 s), $^{19}F$ (4 s), $^{27}Al$ (3 s), $^{30}Si$ (3 s), $^{32}S$ (4 s) and $^{35}Cl$ (6 s; counting times in parentheses), with 2 s waiting time after each switch of the magnet. This cycle was repeated 10 times during one analysis for a total analysis duration of 12 min. The mass resolution of ∼7000 (with the contrast aperture at 400 μm, the energy aperture at 40 eV, the entrance slit at 52 μm and the exit slit at 173 μm) meant that complete discrimination of the following mass interferences was achieved: $^{34}S^1H$ on $^{35}Cl$; $^{17}O$ on $^{16}O^1H$; $^{29}Si^1H$ on $^{30}Si$; $^{31}P^1H$ on $^{32}S$. Element concentrations were determined using calibration curves obtained by measuring a set of natural and experimental basaltic glasses (KL2G, Jochum et al., 2006; KE12, Mosbah et al., 1991; VG2, Jarosewich et al., 1980; experimental glasses N72, M35, M40 and M48, Shishkina et al., 2010; Macquarie glasses 47,963 and 25,603, Kamenetsky et al., 2000) under the same analytical conditions at the beginning, middle, and end of the session. These standards span a large range of volatile element concentrations that bracket the volatile contents of the unknowns. Maximum relative errors, based on reproducibility over 10 cycles of analyses, were less than 15% for $CO_2$, 3% for Cl, 4% for S, and 5% for F and $H_2O$.

### 2.5. XANES Analyses

We carried out Fe K-edge XANES (X-ray absorption near-edge structure spectroscopy) on beamline I18 at the Diamond Light Source (DLS), UK. The X-rays were focused with Kirkpatrick-Baez mirrors down to 7 μm (horizontal) × 2 μm (vertical) beam size. The beamline uses a liquid nitrogen-cooled double-crystal monochromator with silicon crystals, and the Si (333) reflection was used to increase the energy resolution. Measurements were performed in fluorescence mode. We used two energy-dispersive Vortex ME-4 silicon drift detectors positioned at 45° to the incident beam: one located directly above the other, and both pointing toward the sample. The sample was positioned so that the normal to the sample surface was at 45° to the incident X-ray beam. Default analytical conditions for XANES at I18 yield a primary beam with photon flux of $10^{12}$ ph/s upstream of the ion chamber; we used a combination of aluminum foils and slit geometries to attenuate the beam to $10^{10}$ ph/s at the sample surface. For MI analyses, the incident X-ray beam was further attenuated with 0.1 mm-thick Al foil to ensure there was no beam damage to the sample (see section below). The energy step sizes and dwell times used are given in Table S1 in Supporting Information S2 (Moussallam, 2023b). All MI XANES spectra were examined for contamination from the olivine host (Figure 1a). Spectra showing any structure in the edge or post-edge region were rejected (see Figure S6 in Moussallam et al., 2014 for an example of a contaminated XANES spectrum).

The effect of sample exposure to focused X-ray beams on iron speciation has been investigated in several studies for a range of sample compositions under a range of beam conditions (e.g., Cottrell et al., 2009, 2018; Moussallam et al., 2014, 2016, 2019; Shorttle et al., 2015). Accordingly, we selected beam attenuation conditions to eliminate beam damage. To test our analysis conditions, we performed a beam damage test on a SWIR glass containing 0.45 wt.% $H_2O$ (the highest water content in the samples investigated in this study). We positioned the monochromator at a fixed energy of 7114.3 eV corresponding to the oxidized peak of the pre-edge doublet. We then opened the shutter and counted the fluoresced X-rays every second for 700 s (Figure 1c). Under our analytical conditions,

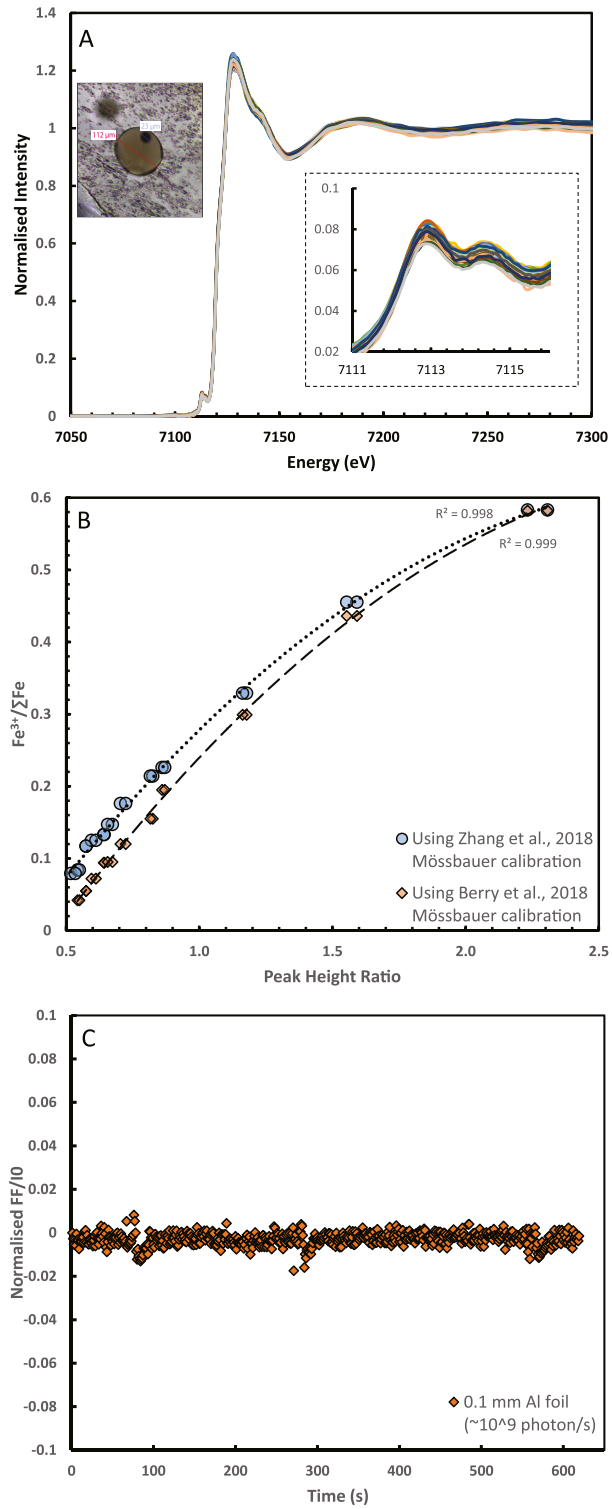


**Figure 1.** (a) Edge step-normalized XANES spectra of SWIR MIs ($n$ = 38) and glasses ($n$ = 5). The lower right inset shows spectra over the pre-edge region energy range. Upper left inset shows a transmitted light photomicrograph of a typical olivine-hosted MI. (b) Calibration line of the peak height ratio determined by XANES compared with $Fe^{3+}/\sum Fe$ ratios determined by Mössbauer spectroscopy in basaltic standard glasses from the Smithsonian NMNH (Mössbauer $Fe^{3+}/\sum Fe$ values from Zhang et al. (2018) and Berry et al. (2018) are shown). (c) Time series of normalized fluoresced intensity (FF) over I0 at 7114.3 eV integrated over 1 s intervals for a SWIR glass containing 0.45 wt.% $H_2O$.

0.1 mm-thick Al foil was used to attenuate the beam to ~16% of its original flux (calculated based on theoretical absorption, equivalent to ~$10^9$ photon/s or ~$10^8$ photon/s/μm$^2$), and we detected no change in fluoresced intensity under beam exposure indicating that Fe in our natural samples was not oxidized during XANES analyses.

The pre-edge region (7110–7118 eV) was fitted using a combination of a linear function and a damped harmonic oscillator function (DHO) to fit the baseline. The relative intensity at the ~7112.5 eV and ~7114.3 eV peaks was then used to calibrate the spectra to the published $Fe^{3+}/\sum Fe$ ratios of the NMNH 117393 basalt reference glasses (Cottrell et al., 2009) loaned by the Smithsonian Institution National Museum of Natural History and using the $Fe^{3+}/\sum Fe$ values reported in Zhang et al. (2018) and in Berry et al. (2018) (Figure 1b). Repeat measurements of standards ($n = 12$) gave a standard deviation of ±0.004 on the measured $Fe^{3+}/\sum Fe$ ratios (relative error). Absolute error is estimated at ±0.005, based on absolute deviation between theoretical (i.e., Mössbauer values) and measured standard values.

### 2.6. LA-ICP-MS Analyses

Trace element measurements on MIs, embayments (partially entrapped melt that remained opened to the outside melt in one direction; also called re-entrants), and glasses were carried out using a laser ablation system (193 nm Excimer RESOlution SE) associated with an inductively coupled plasma mass spectrometer (Agilent 8900 QQQ ICP–MS) at the Institut des Sciences de la Terre d'Orléans (ISTO), France. Analyses were performed following conventional procedures (e.g., Le Voyer et al., 2010; Moussallam et al., 2019b; Rose-Koga et al., 2012). We used a pulse energy of about 5 mJ, a spot diameter between 32 and 100 μm, depending on the inclusion size and a laser pulse frequency of 2–3 Hz to keep a fluence at the sample surface of 2.8 J/cm$^{-2}$. The background was measured for 30–40 s before ablation, and the analysis time was approximately 100 s. Data reduction was performed using GLITTER software (www.es.mq.edu.au/GEMOC). This technique uses calcium (CaO measured by EPMA) as an internal standard. Reproducibility was constrained by systematic analyses of two external standards, BCR2-G (<4% on all elements except Be, Sn and Ta <7%, 1$\sigma$ relative) and NIST-SRM-610 (<3% on all elements except Li <4%, 1$\sigma$ relative), measured at the beginning, middle and end of the session.

## 3. Results

The major element compositions (by EMPA) and volatile contents (by SIMS) of 80 MIs, 2 embayments and 13 matrix glasses were obtained; the $Fe^{3+}/\sum Fe$ ratio was measured (by XANES) in 38 of these MIs and five of these matrix glasses; and trace element concentrations (by LA-ICP-MS) were measured in 31 of these MIs and four of these matrix glasses.

### 3.1. Major Elements

The major element compositions of MIs, embayments, and matrix glasses are given in Table S2 in Supporting Information S2 (Moussallam, 2023b) together with MI and bubble dimensions. The major element compositions of the host crystals (olivine and plagioclase) are given in Table S3 in Supporting Information S2 (Moussallam, 2023b).

The SWIR matrix glass composition appears to be very different from that of the MIs. The glass is much richer in FeO and $TiO_2$, and has lower CaO, $Al_2O_3$ and $SiO_2$ (Figure 2). The olivine forsterite content at equilibrium with the matrix glasses ($Fo_{80\pm1}$) was calculated following Toplis (2005) at a temperature of 1200°C, at 50 MPa, $Fe^{3+}/\sum Fe$ ratio of 0.15 and the measured water content of 0.44 ± 0.06 wt.% (see next section). According to these calculations the matrix glass is far from equilibrium with the olivine (Figures 2j and 2k). Interestingly, the embayments are also different from the matrix glasses, with one embayment having a composition very similar to that of the MIs and one having a composition midway between the MIs and the matrix glass, suggesting mixing of two magmas.

In order to determine if a crystallization relationship existed between the matrix glass and the MIs, we performed a series of fractional crystallization calculations using MELTS v1.2.0 (Ghiorso & Sack, 1995). About 20 MI were randomly picked as starting compositions for the calculation, and four scenarios were tested:

1. Sea floor crystallization: isobaric (15 MPa), cooling from MELTS liquidus to 1050°C—equilibrium crystallization.
2. Sea floor crystallization: isobaric (15 MPa), cooling from MELTS liquidus to 1050°C—fractional crystallization.

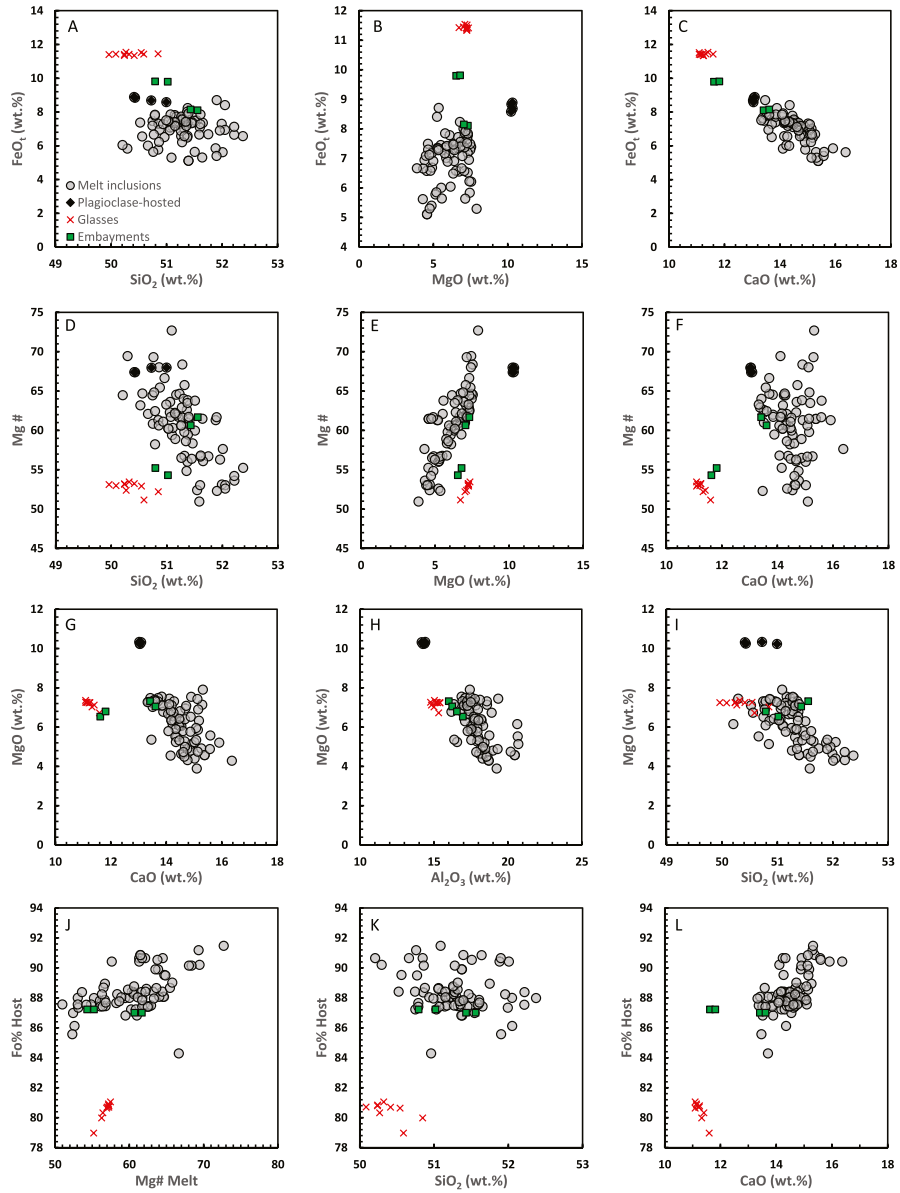


**Figure 2.** Comparison between major element oxides in MIs and matrix glasses from SWIR. The corresponding Fo% for matrix glasses was calculated using the model of Toplis (2005) at a temperature of 1200°C, 50 MPa, $Fe^{3+}/\sum Fe$ ratios of 0.15 and their measured water content. The two embayment compositions were measured at both of their extremities (i.e., the furthest inside and at the mouth).

3. Deep crystallization: isobaric (at MI volatile saturation pressure), cooling from MELTS liquidus to 1050°C—equilibrium crystallization.
4. Deep crystallization: isobaric (at MI volatile saturation pressure), cooling from MELTS liquidus to 1050°C—fractional crystallization.

Results from all four scenarios are shown in Figure S2 in Supporting Information S1 (Moussallam, 2023c) but in none can the glass composition be derived from the MI compositions. All these observations suggest that the carrier melt was unrelated to the MI population and brought to the seafloor a mostly xenocrystic crystal cargo, potentially following an episode of mixing short enough that embayments sample an unhomogenized melt.

Olivine-hosted MIs have compositions that are unusual when compared with the global MORB database (Figure 3). They record a large spread in MgO from 8 to 4 wt.%, and at any given value of MgO, they have lower

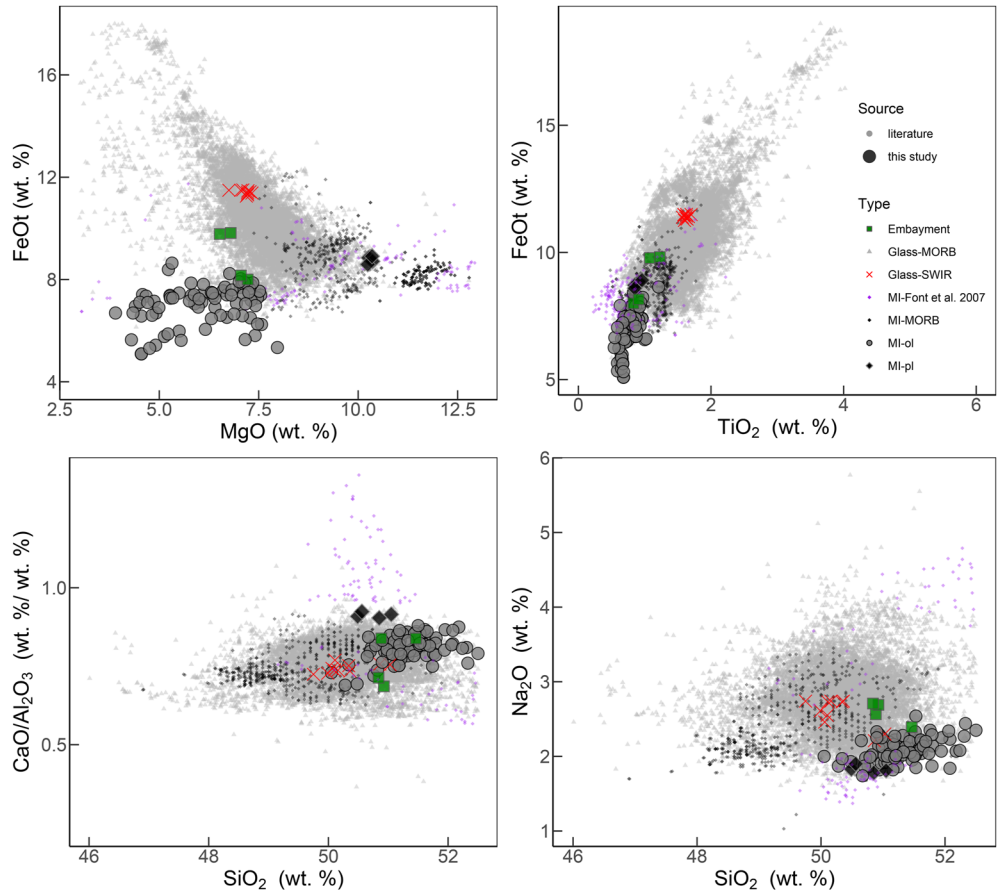


**Figure 3.** Composition of magmatic MIs compared to global MORB glass data ($n$ = 13,773; PETDB and GEOROC databases), and known MORB MIs ($n$ = 542; M. Le Voyer et al., 2017; Saal et al., 2002; Shaw et al., 2008; Shimizu et al., 2019; Wanless & Shaw, 2012; Wanless et al., 2014). MI compositions from SWIR by Font et al. (2007) are shown in purple. The host lava compositions of this study are in red crosses and the compositions of embayments are in green squares. Although the MIs of this study are notably low in MgO and FeOt, similar compositions have been reported previously. (a) FeO total versus MgO, (b) FeO total versus $TiO_2$, and note that the MIs are low in both. (c) $CaO/Al_2O_3$ versus $SiO_2$, showing that the MI compositions plot within the global distribution. (d) $Na_2O$ versus $SiO_2$ showing $Na_2O$ is at the lower end of the global population.

$TiO_2$, FeOt, and $Na_2O$ with comparable $CaO/Al_2O_3$ compared to the global MORB database. Similar compositions were found by Font et al. (2007) in olivine-hosted inclusions from other MORB samples dredged along the South West Indian Ridge, but their study focused more on plagioclase-hosted MIs with reported compositions similar to those we report here (Figure 3). $Na_2O$, $TiO_2$, and MgO are at the lower end of the global MORB population. The low $Na_2O$, $TiO_2$, and MgO cannot be derived from crystal fractionation of typical MORB magmas as $Na_2O$ and $TiO_2$ generally increase with crystal fractionation, which typically decrease MgO concurrently.

### 3.2. Trace Elements

The trace element compositions of MIs and matrix glasses are given in Table S4 in Supporting Information S2 (Moussallam, 2023b). Trace element systematics can distinguish between fractional crystallization, mixing, or partial melting genetic processes (e.g., Allègre & Minster, 1978; Schiano et al., 2010; Treuil, 1975). From the co-evolution of La and Rb, two highly incompatible elements (Figure 4a), we identify a linear correlation that does not pass through the origin. This observation is consistent with mixing or potentially a partial melting origin but inconsistent with the melts being related to different degrees of fractional crystallization (which would produce a linear trend passing through the origin). In a $C^H/C^M$ versus $C^H$ diagram (where $C^H$ and $C^M$ are the concentrations of highly incompatible and moderately incompatible elements respectively) (Figure 4b) we observe a linear correlation, consistent with partial melting or potentially a mixing origin but inconsistent with

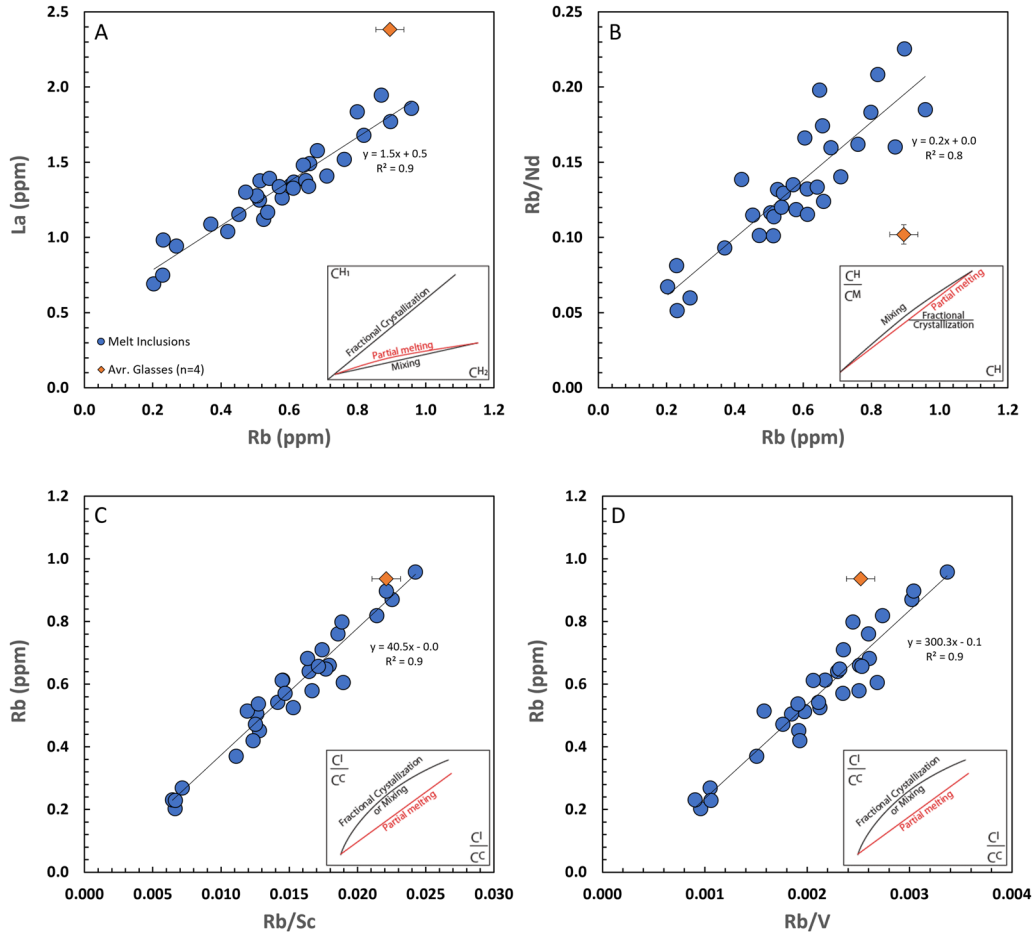


**Figure 4.** Trace element variation diagrams from MIs and average values of matrix glasses from SWIR. (a) Plot of La versus Rb with inset showing a schematic $C^{H1}$ versus $C^{H2}$ diagram (with $H_1$ and $H_2$ being two highly incompatible elements) with curves showing theoretical melt compositions produced by fractional crystallization, partial melting, and mixing processes. (b) Plot of Rb/Nd versus Rb with inset showing a schematic $C^H/C^M$ versus $C^H$ diagram (where $C^H$ and $C^M$ are the concentrations of H, a highly incompatible element, and M, a moderately incompatible element) showing theoretical correlation curves during fractional crystallization, partial melting and mixing processes. (c) Plot of Rb versus Rb/Sc, with inset showing a schematic $C^I$ versus $C^I/C^C$ diagram (where $C^I$ and $C^C$ are the concentrations of I, an incompatible element, and C, a compatible element) showing theoretical melt compositions produced by mixing, fractional crystallization and partial melting processes. (d) The plot of Rb versus Rb/V. All inset schematics were redrawn from Schiano et al. (2010). Linear regressions through all MI data are presented on each plot.

the melts being related to different degrees of fractional crystallization (which would produce a near-horizontal line). In a $C^I$ versus $C^I/C^C$ diagram (where $C^I$ and $C^C$ are incompatible and compatible elements respectively) (Figures 4c and 4d), we observe a linear correlation consistent with partial melting but inconsistent with the melts being related to either different degrees of fractional crystallization or by mixing (both of which would produce a hyperbolic curve). The trace element systematics in the SWIR MIs therefore suggest that the melts are related to variable degrees of partial melting. The trace element analyses also reinforce the observation made from the major elements, that the carrier melt is compositionally distinct from the MI population.

### 3.3. Volatile Elements

The volatile contents of MIs, embayments and matrix glasses are given in Table S2 in Supporting Information S2 (Moussallam, 2023b) together with calculated volatile ($H_2O$-$CO_2$) saturation pressures using the model of Iacono-Marziano et al. (2012). Additional SIMS analyses along the two olivine-hosted melt embayments are reported in Table S5 in Supporting Information S2 (Moussallam, 2023b). MIs span a range of concentrations from 68 to 1400 ppm $CO_2$, from 0.30 to 0.39 wt.% $H_2O$, and from 540 to 1150 ppm S, while the matrix

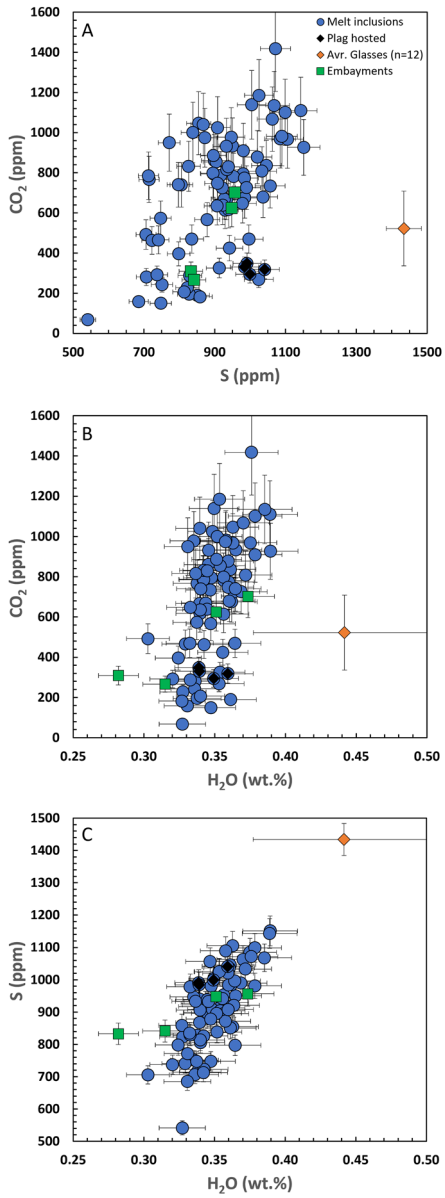


**Figure 5.** Volatile element abundances in MIs, embayments and matrix glasses from SWIR. Plagioclase-hosted MIs are marked by black diamond symbols, and all other MIs are olivine-hosted. The two embayments were measured at both of their extremities (i.e., the furthest inside and at the mouth). Error bars show one standard deviation from measurement uncertainty except for the average matrix glass where error bars show one standard deviation from $n = 12$ analyses.

glass contains on average 500 ± 200 ppm $CO_2$, 0.44 ± 0.06 wt.% $H_2O$ and 1400 ± 50 ppm S (averages and one standard deviation on $n = 12$ analyses) (Figure 5). The volatile element concentrations provide additional evidence supporting the conclusion, based on major and trace elements, that the carrier melt is markedly different from the MIs.

Calculated volatile ($H_2O$-$CO_2$) saturation pressures range from 22 to 316 MPa for MIs, corresponding to minimum entrapment pressures down to ~10.5 km below the sea floor. For matrix glasses, calculated volatile ($H_2O$-$CO_2$) saturation pressures range from 89 to 214 MPa (average ~115 ± 41 MPa), which is much higher than the ~26 MPa hydrostatic pressure expected at the sample collection depth of ~2650 m b.s.l. (where the expected $CO_2$ content in the glass would be around ~90 to 70 ppm). This volatile supersaturation in the glass is significantly higher than that seen in most MORBs (see Figure 5a in Aubaud, 2022) and suggests rapid melt ascent with kinetically limited $CO_2$ exsolution and small bubble number density preventing efficient degassing (e.g., Gardner et al., 2016; Pichavant et al., 2013). Diffusion profile modeling of the two olivine-hosted embayments (using the EMBER software; Georgeais et al., 2021) yields a decompression rate of 0.001–0.005 MPa/s (Table S6 in Supporting Information S2; Moussallam, 2023b).

### 3.4. Oxidation State

The Fe oxidation states of 38 MIs and five matrix glasses measured by XANES are reported in Table S2 in Supporting Information S2 (Moussallam, 2023b) and shown in Figure 6. MI $Fe^{3+}/\Sigma Fe$ ranges from 0.147 to 0.172, with an average of 0.160 and standard deviation of ±0.006. Matrix glass $Fe^{3+}/\Sigma Fe$ ranges from 0.143 to 0.152, with an average of 0.149 and standard deviation of ±0.004. Here and in all figures and remaining text we report $Fe^{3+}/\Sigma Fe$ for our analyses based on the calibration using Mössbauer values from Zhang et al. (2018) for the Smithsonian reference glasses. For comparison, we also report the corresponding $Fe^{3+}/\Sigma Fe$ values using the calibration based on Mössbauer data from Berry et al. (2018) for the reference glasses (termed "$Fe^{3+}/\Sigma Fe$ $^{2}$" in Table S2 in Supporting Information S2; Moussallam, 2023b). Conversion to deviation from the QFM buffer was performed following Kress and Carmichael (1991) at a fixed pressure of 26 MPa, with individual olivine-hosted MI temperatures estimated using the olivine-melt equilibrium model of Danyushevsky (2001) and plagioclase-hosted MI and matrix glass temperatures estimated using the MORB glass geothermometer of Wallace and Carmichael (1992). This is the ΔQFM value we use in all figures and remaining text. For comparison, in Table S2 in Supporting Information S2 (Moussallam, 2023b) we also report conversion to deviation from the QFM buffer using the equation of O'Neill et al. (2018), termed "ΔQFM $^{2}$," which uses "$Fe^{3+}/\Sigma Fe$ $^{2}$" as input.

MIs range from $\log(fO_2) = QFM-0.17$ to +0.02 with an average of −0.07 and standard deviation of ±0.05. Matrix glasses range from $\log(fO_2) = QFM-0.22$ to −0.05 with an average of −0.11 and standard deviation of ±0.06. It is worth re-stating that the relative precision of our XANES analyses is ±0.004 on the measured $Fe^{3+}/\sum Fe$ ratio. MIs show no correlation between their $Fe^{3+}/\sum Fe$ ratios and their volatile element contents ($CO_2$, S, and $H_2O$; Figures 6a–6c). This remains the case when the $Fe^{3+}/\sum Fe$ ratios are converted to deviation from the QFM buffer (i.e., accounting for melt composition and temperature) (Figures 6n and 6o). Correlations do emerge between the measured $Fe^{3+}/\sum Fe$ ratios and the major element compositions, most notably with MgO, CaO, and $SiO_2$ contents ($R^2$ values of 0.6, 0.4 and 0.5 respectively, Figures 6d–6f). However, once converted to deviation from the QFM buffer none of these correlations remain ($R^2$ values of 0.0; Figures 6p–6r). The MI $Fe^{3+}/\sum Fe$ ratios are uncorrelated with olivine host

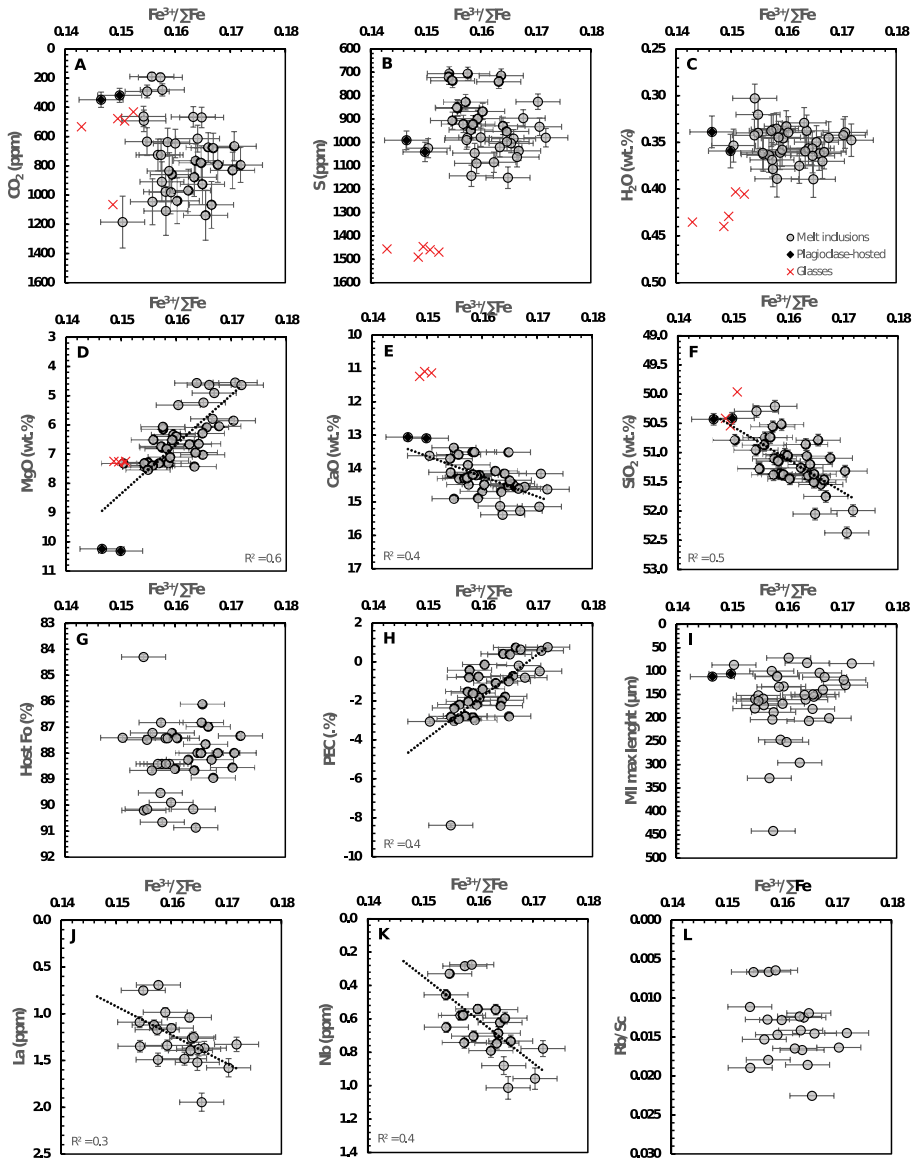


**Figure 6.** Oxidation states of SWIR MIs and glasses measured by Fe-XANES expressed as measured $Fe^{3+}/\Sigma Fe$ (panel A to L) and corresponding oxygen fugacity expressed as log unit deviation from the QFM buffer (panel N to X).

composition and inclusion size (Figures 6g and 6i) but are correlated with the calculated amount of post entrapment crystallization ($R^2 = 0.4$; Figure 6h). This correlation also disappears once converted to deviation from the QFM buffer ($R^2 = 0.0$; Figure 6t). Finally, correlations between $Fe^{3+}/\sum Fe$ ratios and trace elements such as La or Nb ($R^2$ values of 0.3 and 0.4 respectively, Figures 6j and 6k) also disappear once converted to deviation from the QFM buffer ($R^2 = 0.0$; Figures 6v and 6w). The oxidation states of MIs and matrix glasses from the South West Indian Ridge hence appear extremely uniform despite the large range in major, trace and volatile element concentrations they record.

## 4. Discussion

### 4.1. Fast Magma Ascent Rate and Minimal Chemical Exchange

As shown above (IIIa,b,c), the matrix glass composition is distinct from that of the MIs, suggesting that the carrier melt was unrelated to the MI population and brought to the seafloor a mostly xenocrystic crystal cargo.

10.1029/2023GC011235

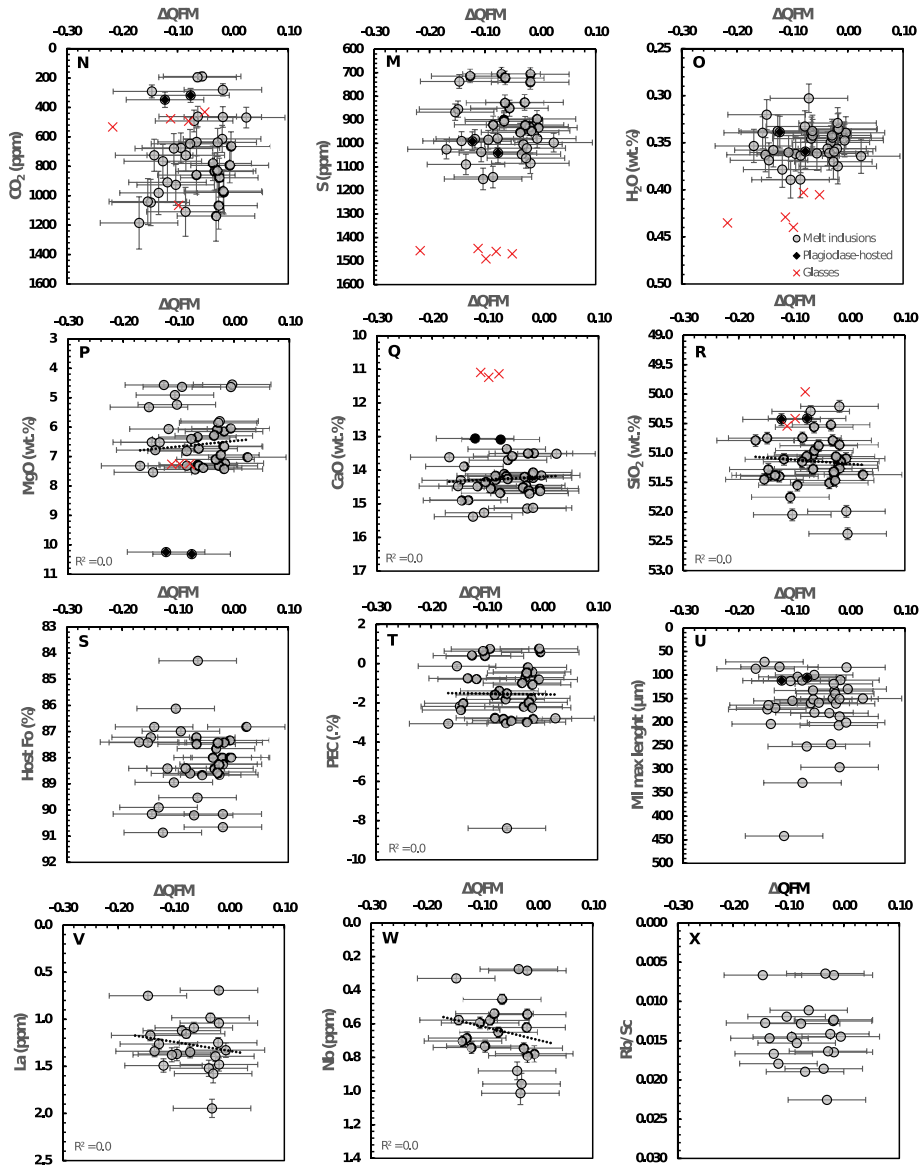


**Figure 6.** (Continued)

The eruption must have taken place following an episode of mixing short enough not to homogenize the embayment compositions. Such dynamic conditions suggest an explanation for the apparent uniformity in the oxidation state recorded in MIs, namely that any initial redox heterogeneity was overprinted by re-equilibration with the carrier melt via hydrogen diffusion through the olivine hosts, which can occur on timescales of hours to days (Gaetani et al., 2012).

In order to test this scenario, we first modeled the volatile diffusion profiles recorded in two olivine-hosted melt embayments using the EMBER software (Georgeais et al., 2021) to determine the rate and duration of magma ascent (results in Tables S5 and S6 in Supporting Information S2; Moussallam, 2023b). We then modeled MI re-equilibration through hydrogen diffusion using the MATLAB routine of Bucholz et al. (2013). The results suggest that the SWIR magma experienced 5–13 hr of ascent at a rate of 0.03–0.19 m/s (decompression rate of 0.001–0.005 MPa/s; we neglect acceleration) (Figure 7). In contrast, the MI $fO_2$ re-equilibration timescale was calculated to be about 80 hr with no change in the MI $fO_2$ in the first 5 hr and little in the first 20 hr (Figure S3 in Supporting Information S1; Moussallam, 2023c). Moreover, if hydrogen diffusion re-equilibration had occurred between MIs and the carrier melt then a relation between the water content and $fO_2$ of the MIs would

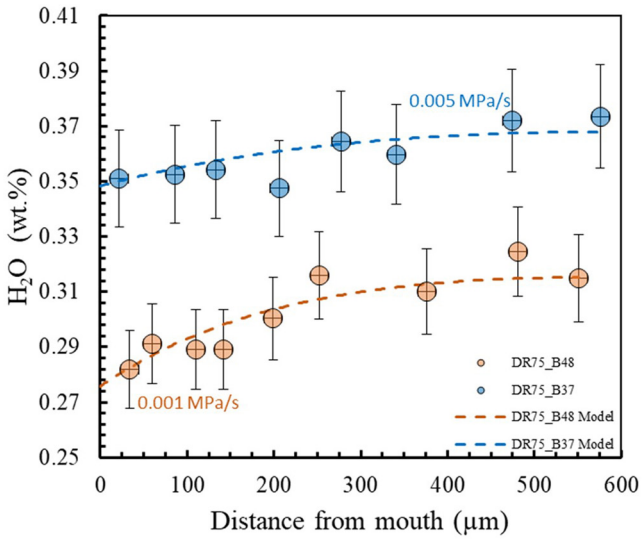


**Figure 7.** Best-fit diffusion modeling results (calculated using EMBER; Georgeais et al., 2021) compared to $H_2O$ concentrations (measured by SIMS) for two SWIR melt embayments.

be expected, as would a relation between MI size and water content (the smaller MI being more sensitive to $H_2O$ loss), neither of which was evident in our data ($R^2 = 0.0$, Figure S3 and Table S2 in Supporting Information S2; Moussallam, 2023b, 2023c). Finally, the fact that both plagioclase- and olivine-hosted MIs as well as open melt embayments all record similar redox conditions suggests that the Fe-system was not disturbed after MI entrapment.

We consider that the buffering/re-equilibration and post-entrapment modification of the SWIR MI $fO_2$ during ascent is thus unlikely to have been significant, and therefore the inclusions retain their original $fO_2$ at the time of entrapment. We cannot entirely exclude the possibility that the MIs equilibrated with yet another melt or magmatic environment at depth prior to their entrainment in the carrier melt that transported them to the surface, but such a scenario would imply the presence of an additional distinct magma which is not found, and should again have resulted in relations between the size, water content and $fO_2$ of the MIs which are not evident.

### 4.2. A New Series of $CO_2$-Undersaturated, Undegassed Melts

MI $CO_2$ contents are correlated with other highly incompatible elements such as Ba ($R^2 = 0.5$), Rb ($R^2 = 0.4$) and Nb ($R^2 = 0.4$), which indicates that these MIs did not lose their initial carbon through degassing (Figure 8). MI $CO_2$ and Cl contents are also strongly correlated ($R^2 = 0.8$). This is a strong indication that the MIs have not been contaminated by seawater, and that both elements behaved as incompatible elements and were unaffected by degassing.

The $CO_2$/Ba ratio in SWIR MIs is 123 ± 32, consistent with a depleted mantle value of ∼140 (Matthews et al., 2017) but slightly higher than the 100 ± 22 ratio found in the Siqueiros MIs (Saal et al., 2002), the 97 ± 10 ratio found in the equatorial MIs (M. Le Voyer et al., 2017) and the 76 ± 8 ratio found in the 2πD43 popping rock (Cartigny et al., 2008). The $CO_2$/Rb and $CO_2$/Nb ratios in SWIR MIs (1,374 ± 487 and 1,134 ± 415 respectively) are also higher than the those found in the Siqueiros MIs (∼1,219 and 239 ± 46 respectively), equatorial MIs (1,105 ± 104 and 557 ± 79 respectively), and in the 2πD43 popping rock (899 ± 91 and 556 ± 56 respectively) (Cartigny et al., 2008; M. Le Voyer et al., 2017; Saal et al., 2002). The $CO_2$/Cl ratio in SWIR MIs is 78 ± 15, similar to the 77 ± 26 ratio found in the Siqueiros MIs (Saal et al., 2002) and higher than the ratio of 46 found in the Popping Rock (sample 2πD43; Cartigny et al., 2008), and the 39 ± 4 ratio found in the equatorial MIs (M. Le Voyer et al., 2017). We note that the SWIR matrix glasses also show $CO_2/C_{ITE}$ ratios significantly higher than other MORBs, which appears consistent with $CO_2$ being undersaturated in the matrix glass.

Unlike $CO_2$, the water and sulfur contents of the MIs are uncorrelated with incompatible trace elements (ITE) such as Ce and Dy, respectively ($R^2 = 0.2$). Sulfur abundance in MORBs is widely considered to be controlled by equilibrium with sulfide (e.g., Jenner et al., 2010; Mathez, 1976; O'Neill, 2021; Shimizu et al., 2019). One MI in our suite was found to contain a sulfide globule, and sulfide inclusions were also found in olivine crystals and in the matrix glass, indicating sulfide saturation for at least some and probably most of the melt evolution pathway. The sulfur abundance in the SWIR MIs is not well correlated with their $FeO_t$ contents ($r^2 = 0.3$) but is comparable (on average within 19 ± 15% or 165 ± 140 ppm) to the predicted sulfur concentrations at sulfide saturation, calculated following O'Neill (2021). Taken together, these observations suggest that the melt S content was at least partially dictated by equilibrium with sulfide liquid. The positive correlation between water and sulfur content ($R^2 = 0.5$) would be expected if both species had been affected by degassing, as is commonly seen in MI suites from subaerial volcanoes (e.g., Stromboli; Métrich et al., 2005). The $CO_2$-undersaturated nature of our SWIR MI suite should inhibit any significant S and $H_2O$ degassing at >26 MPa pressure. Yet, for water at least, diffusion profiles recorded in melt embayments indicate that some degassing took place (see section a).

### 4.3. $CO_2$ Content of the Mantle Source

Experimental work indicates that incompatible element ratios such as $CO_2$/Nb and $CO_2$/Ba remain nearly constant during mantle melting and fractional crystallization (Rosenthal et al., 2015). If the initial trace element content

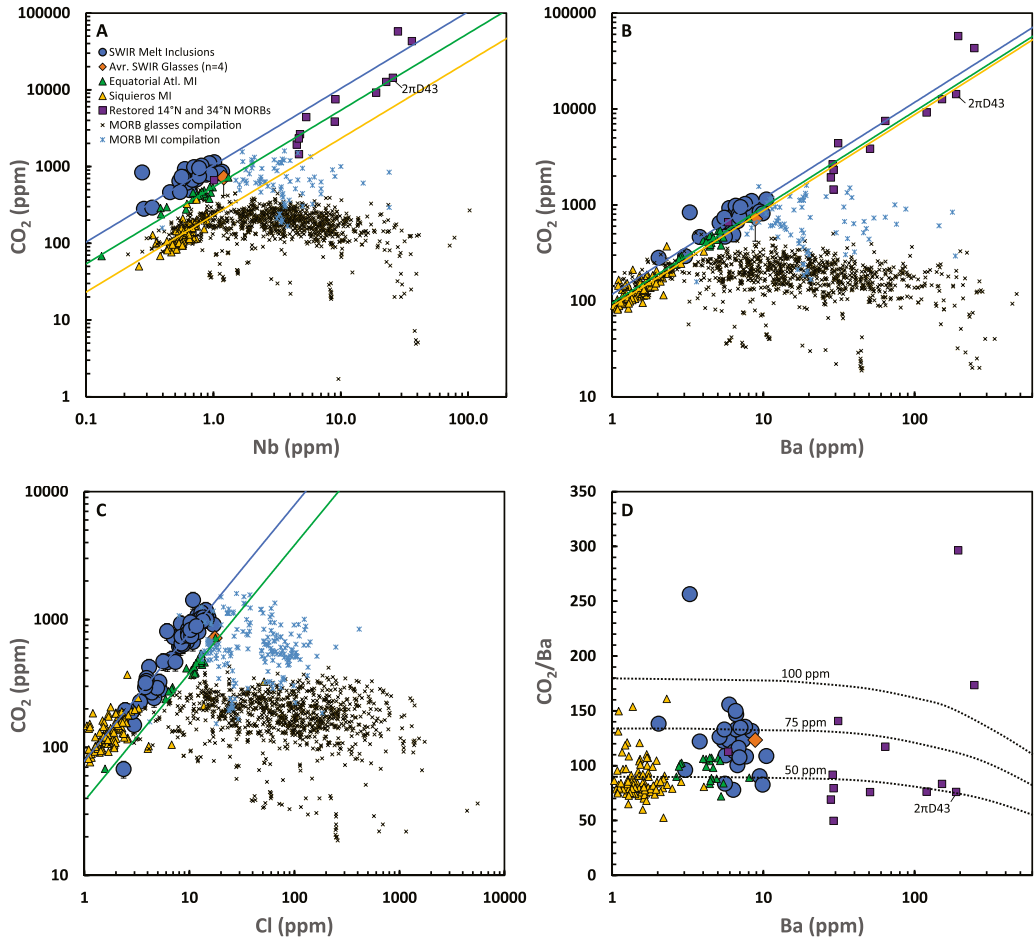


**Figure 8.** $CO_2$ versus Nb, Ba and Cl (A–C) and $CO_2$/Ba versus Ba (D) for MIs and matrix glasses from this study (SWIR) and previous studies of $CO_2$-undersaturated MIs and glasses. Equatorial Atlantic MIs are from Le Voyer et al. (2017). Siqueiros MIs are from Saal et al. (2002). 14°N and 34°N mid-Atlantic ridge $CO_2$ contents are reconstructed values from Cartigny et al. (2008). Sample 2πD43 is the popping rock (Cartigny et al., 2008). MORB glasses and MORB MI compilations showing partially to mostly degassed samples are from Le Voyer et al. (2017) and references therein. Solid blue, green, and yellow lines represent regressions forced through the origin for the SWIR, equatorial Atlantic and Siqueiros MI suites respectively. Dotted black curves in D are calculated partial melt compositions by Rosenthal et al. (2015) from simple batch melting, using their partition coefficients and assuming a mantle source with Ba = 0.563 ppm (Workman & Hart, 2005), and 50, 75, and 100 ppm $CO_2$.

of the mantle source is known, its $CO_2$ content can be derived. Several estimates of mantle source trace element compositions are found in the literature. For example, assuming a depleted MORB mantle (DMM) source composition with Ba = 0.563 ppm, Rb = 0.050 ppm, and Nb = 0.1485 ppm (values from Workman & Hart, 2005) would give mantle $CO_2$ abundances of 69 ± 18 ppm (from $CO_2$/Ba), 69 ± 24 ppm (from $CO_2$/Rb), and 168 ± 62 ppm (from $CO_2$/Nb). Using an alternative DMM Nb content of 0.3 ± 0.05 ppm (as quoted in Saal et al., 2002) would give a mantle $CO_2$ abundance of 340 ± 124 ppm (from $CO_2$/Nb).

Previous studies do not always clearly indicate which mantle source composition (i.e., Nb, Ba, Rb content) was used to calculate mantle $CO_2$ content, making comparison between our study and previous estimates difficult. Another difficulty is that some studies base calculations on the average $CO_2/C_{ITE}$ ratio measured in a suite of samples, while others use single or highest values. Previous estimates of the mantle source region of MORBs vary from ~20 to 1200 ppm $CO_2$ (e.g., Cartigny et al., 2008; Chavrit et al., 2014; Hauri et al., 2018; Helo et al., 2011; Hirschmann, 2018; Javoy & Pineau, 1991; Le Voyer et al., 2019; Marty & Jambon, 1987; Saal et al., 2002). To make the comparison with previous studies easier, Figure 8d presents the $CO_2$/Ba versus Ba content calculated

for partial melting of a mantle containing 50, 75, or 100 ppm $CO_2$ (after Rosenthal et al., 2015, using mantle Ba = 0.563 ppm) with the values measured in the SWIR, equatorial Atlantic (Le Voyer et al., 2017) and Siqueiros (Saal et al., 2002) MI series and in the popping rock and the reconstructed 14°N and 34°N mid-Atlantic ridge MORBs (Cartigny et al., 2008). Using a Ba mantle value of 0.563 ppm, a mantle $CO_2$ content between 25 and 100 ppm appears most consistent with all these studies, with the SWIR series potentially indicating slightly higher $CO_2$ in its source compared with the equatorial Atlantic and Siqueiros series.

### 4.4. The Behavior of $Fe^{3+}$ During Partial Mantle Melting

In most MI and matrix glass suites where oxidation state has been measured, degassing, especially of sulfur species, has been shown to strongly influence the melt oxidation state (Brounce et al., 2017; Hartley et al., 2017; Helz et al., 2017; Moussallam et al., 2014, 2016, 2019; Shorttle et al., 2015), which is also strongly influenced by the removal of chalcophile elements, for example, by sulfide saturation (Jenner et al., 2010). The $CO_2$-undersaturated MI suite from SWIR, in which S degassing is unlikely to have occurred (and S content is uncorrelated with oxidation state), thus presents an opportunity to consider processes other than degassing which might influence the melt oxidation state.

$Fe^{3+}$ is expected to behave incompatibly to moderately incompatibly during mantle partial melting (e.g., Davis & Cottrell, 2021; Gaetani, 2016; Ghiorso et al., 2002; Jennings & Holland, 2015; Sorbadere et al., 2018), leading to lower $Fe_2O_3$ contents in higher degree partial melts (e.g., pyroxene/melt $Fe^{3+}$ partitioning experiments of Rudra & Hirschmann, 2022). The undegassed SWIR MIs show variable enrichment in incompatible elements, consistent with origin by variable amounts of partial melting (see result section b). They would therefore be predicted to display a positive correlation between $Fe^{3+}$ and incompatible trace element concentrations.

Because the MIs have all been entrapped at different stages during crystallization, their composition and $Fe^{3+}/\Sigma Fe$ need first be corrected. We modeled reverse crystallization paths for our olivine-hosted MIs along olivine control lines using PRIMELT3 (Herzberg & Asimow, 2015) until the melts reached 10 wt.% MgO (Figure 9a). We further estimated the degree of partial melting necessary to produce these melts. We used PRIMELT3 olivine fractionation results to estimate ITE concentrations at 10 wt.% MgO using the olivine-melt partition coefficients of McKenzie and O'Nions (1991). We then calculated the degree of partial melting necessary to reproduce each melt Rb concentration, assuming a source with Rb = 0.050 ppm and bulk partition coefficients of 0.00001 (values from Workman & Hart, 2005). Neither corrected (at MgO = 10 wt.%) nor raw $Fe^{3+}/\Sigma Fe$ shows any correlation with incompatible trace element abundance, incompatible trace element ratios such as Ba/La or estimated degree of partial melting (Figures 9b–9d).

The SWIR MI suite therefore does not show any evidence supporting a simple incompatible behavior of $Fe^{3+}$ during partial melting of the upper mantle. If $Fe^{3+}$ was behaving incompatibly, then one would expect a change in $Fe^{3+}/\Sigma Fe$ during mantle partial melting, such as shown by Gaetani (2016). The Gaetani (2016) model's initial assumption is that no electron transfer is possible between the melt and residual peridotite, forcing the conservation of $Fe^{3+}$ and $Fe^{2+}$ in the system. Gaetani (2016) predicts a change of $Fe^{3+}/\Sigma Fe$ from 0.07 to 0.12 over 12% of partial melting at 1346 ˚C mantle temperature. SWIR MIs show a range of $Fe^{3+}/\Sigma Fe$ from 0.13 to 0.15 (at MgO = 10 wt.%) and no significant geochemical systematics (Figures 9b and 9c).

Our observations are not the first to contradict a simple incompatibility model for $Fe^{3+}$. Bézos and Humler (2005) found a negative correlation between $Fe_2O_3$ and Na (corrected for fractional crystallization at MgO = 8 wt.%) in MORB glasses, which was later confirmed by Cottrell and Kelley (2011). To reconcile our and previous natural observations with experimental evidence for an incompatible behavior of $Fe^{3+}$ during mantle partial melting of the mantle, we propose two non-mutually exclusive hypotheses. The first is that the oxidation state of partial mantle melts is buffered by the subsolidus mantle rather than dominated by an invariant initial budget of $Fe^{3+}$. Hydrogen, given its mobility in mineral phases and melts at upper mantle temperatures, would likely be the primary agent of electron transfer, giving the mantle a redox buffering capacity and forcing all partial melts to maintain a constant redox state near FMQ = 0. The second hypothesis, as proposed by Cottrell and Kelley (2011) and shown by Sorbadere et al. (2018), is that the bulk peridotite-melt partition coefficient of $Fe_2O_3$ ($D^{\text{Peridotite-melt}}_{Fe_2O_3}$) might not be constant but decreases with increasing degree of partial melting, hence causing the melt $Fe^{3+}/\Sigma Fe$ to remain constant over variable degrees of partial melting. Davis and Cottrell (2021) provided additional evidence for this by characterizing the temperature dependency of the spinel-melt partition coefficient (decreasing with increasing temperature).

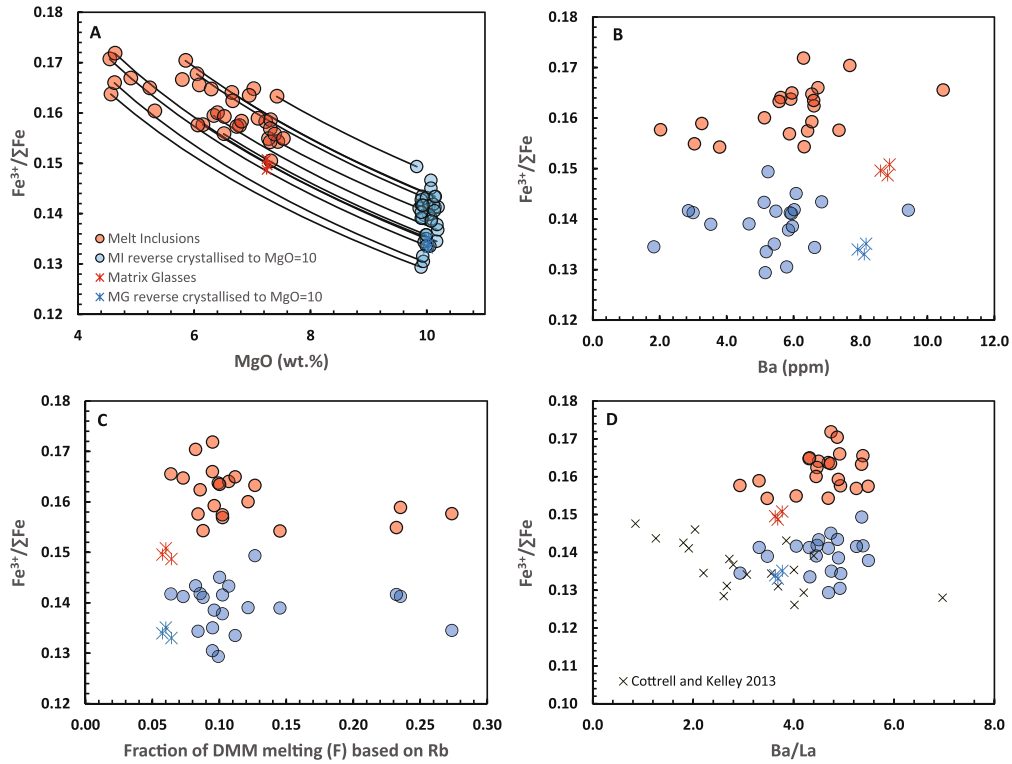


**Figure 9.** (a) Modeled reverse crystallization paths for SWIR olivine-hosted MIs along olivine control lines using PRIMELT3 (Herzberg & Asimow, 2015) until the melts reach 10 wt.% MgO. Solid black lines show reverse crystallization paths for a subset of inclusions. (b) Raw (red) and corrected to MgO = 10 wt.% (blue) $Fe^{3+}/\Sigma Fe$ ratios in olivine-hosted MIs compared to their Ba content. (c) Raw and corrected $Fe^{3+}/\Sigma Fe$ ratios compared to the estimated degree of partial melting of a DMM source (note that these calculations are highly assumption-dependent, results are shown only to demonstrate that a range in F is expected). (d) Raw and corrected $Fe^{3+}/\Sigma Fe$ ratios compared to Ba/La. A global dataset from Cottrell and Kelley (2013) is shown for comparison.

## 5. Conclusions

We performed major, trace and volatile element measurements on a series of olivine- and plagioclase-hosted melt inclusions and matrix glasses from MORBs of the South West Indian Ridge, together with X-ray absorption near-edge structure spectroscopy measurements at the iron K-edges. We found that both melt inclusions and matrix glasses show clear signs of $CO_2$ undersaturation, with $CO_2$ positively correlating with incompatible trace elements. The SWIR $CO_2$/Ba (123 ± 32), $CO_2$/Rb (1,374 ± 487) and $CO_2$/Nb (1,134 ± 415) ratios are amongst the highest measured in MORBs, indicating a $CO_2$-rich mantle source containing 69 ± 18 ppm $CO_2$, calculated assuming a source composition with 0.563 ppm Ba.

The melt inclusion trace element systematics are consistent with formation by variable degrees of partial melting, and their volatile contents indicate minimum entrapment pressures equivalent to depths up to 10.5 km below the seafloor (i.e., in the upper mantle). Since the melt inclusions are $CO_2$-undersaturated, they must have experienced extremely limited amounts of volatile degassing, which would have overprinted their initial oxidation state. The melt inclusion oxidation states show no systematic variation with volatile abundance or composition, and external redox buffering by a carrier melt is unlikely given the rapid magma ascent speed of 0.03–0.19 m/s, determined from water diffusion in embayment profiles.

The MI hence offer a unique sample suite to test the behavior of $Fe^{3+}$, which is expected to act as an incompatible element during partial melting. We found no correlation between the melt $Fe^{3+}/Fe_{tot}$ ratio (nor $Fe_2O_3$ content nor oxidation state as ΔQFM) and other incompatible trace elements even after correcting for the effect of olivine crystallization to a common reference point at MgO = 10 wt.%. We find instead that the oxidation state of all melt inclusions is uniform with a $Fe^{3+}/Fe_{tot}$ ratio of 0.160 ± 0.006 (giving $Fe^{3+}/Fe_{tot}$ of 0.140 ± 0.005 at MgO = 10 wt.%), corresponding to $\log(fO_2)$ = QFM−0.07 ± 0.05 (giving $\log(fO_2)$ = QFM−0.30 ± 0.09 at MgO = 10wt.%).

These findings suggest that upper mantle partial melts are effectively buffered by the mantle in which they form/travel or/and that the bulk peridotite-melt partition coefficient of $Fe_2O_3$ decreases with temperature and increasing degree of partial melting, producing melts with essentially constant $Fe^{3+}/\sum Fe$. Current models of the behavior of $Fe^{3+}/\sum Fe$ during partial melting of peridotite may therefore need to be revised. This includes reevaluating the anticipated influence of the extent of mantle partial melting on the oxidation state of volcanic materials and their potential connection to oxygenation of the atmosphere.

## Data Availability Statement

Raw X-ray absorption near-edge structure spectra at the iron K-edge are archived as Moussallam (2023a). Table S1–S6 in Supporting Information S2 are archived as Moussallam (2023b). Figures S1–S3 in Supporting Information S1 and text are archived as Moussallam (2023c).

**Acknowledgments**
Analytical work was carried out at Diamond Light Source using beamline I18 (proposal number SP29542-1) with invaluable support from Konstantin Ignatyev. Samples were provided by the Marine Rock Repository at IPGP (Paris, France, https://lithotheque.ipgp.fr/) and we are most grateful to Catherine Mevel, Javier Escartin and Mathilde Cannat for help in selecting and obtaining them. BS is supported by Labex VOLTAIRE (ANR-10-LABX-100-01). We thank Jean-Luc Devidal for his precious help during the electron probe analysis and Nordine Bouden and Johan Villeneuve for their invaluable support during the ion probe analyses. We thank Hugh O'Neill, Anja Rosenthal and an anonymous reviewer for their comments and suggestions on previous versions of this manuscript, and Marie Edmonds for editorial handling.

## References

Allègre, C. J., & Minster, J. F. (1978). Quantitative models of trace element behavior in magmatic processes. *Earth and Planetary Science Letters*, *38*(1), 1–25. https://doi.org/10.1016/0012-821X(78)90123-1

Aubaud, C. (2022). Carbon stable isotope constraints on $CO_2$ degassing models of ridge, hotspot and arc magmas. *Chemical Geology*, *605*, 120962. https://doi.org/10.1016/j.chemgeo.2022.120962

Berry, A. J., Stewart, G. A., O'Neill, H. S. C., Mallmann, G., & Mosselmans, J. F. W. (2018). A re-assessment of the oxidation state of iron in MORB glasses. *Earth and Planetary Science Letters*, *483*, 114–123. https://doi.org/10.1016/j.epsl.2017.11.032

Bézos, A., & Humler, E. (2005). The Fe3/Sigma Fe ratios of MORB glasses and their implications for mantle melting. *Geochimica et Cosmochimica Acta*, *69*(3), 711–725. https://doi.org/10.1016/j.gca.2004.07.026

Brounce, M., Stolper, E., & Eiler, J. (2017). Redox variations in Mauna Kea lavas, the oxygen fugacity of the Hawaiian plume, and the role of volcanic gases in Earth's oxygenation. *Proceedings of the National Academy of Sciences*, *114*(34), 8997–9002. https://doi.org/10.1073/pnas.1619527114

Bucholz, C. E., Gaetani, G. A., Behn, M. D., & Shimizu, N. (2013). Post-entrapment modification of volatiles and oxygen fugacity in olivine-hosted melt inclusions. *Earth and Planetary Science Letters*, *374*, 145–155. https://doi.org/10.1016/j.epsl.2013.05.033

Cannat, M., Rommevaux-Jestin, C., Sauter, D., Deplus, C., & Mendel, V. (1999). Formation of the axial relief at the very slow spreading Southwest Indian Ridge (49° to 69°E). *Journal of Geophysical Research*, *104*(B10), 22825–22843. https://doi.org/10.1029/1999JB900195

Cartigny, P., Pineau, F., Aubaud, C., & Javoy, M. (2008). Towards a consistent mantle carbon flux estimate: Insights from volatile systematics ($H_2O$/Ce, δD, $CO_2$/Nb) in the North Atlantic mantle (14° N and 34° N). *Earth and Planetary Science Letters*, *265*(3–4), 672–685. https://doi.org/10.1016/j.epsl.2007.11.011

Chavrit, D., Humler, E., & Grasset, O. (2014). Mapping modern $CO_2$ fluxes and mantle carbon content all along the mid-ocean ridge system. *Earth and Planetary Science Letters*, *387*, 229–239. https://doi.org/10.1016/j.epsl.2013.11.036

Cottrell, E., & Kelley, K. A. (2011). The oxidation state of Fe in MORB glasses and the oxygen fugacity of the upper mantle. *Earth and Planetary Science Letters*, *305*(3–4), 270–282. https://doi.org/10.1016/j.epsl.2011.03.014

Cottrell, E., & Kelley, K. A. (2013). Redox heterogeneity in mid-ocean ridge basalts as a function of mantle source. *Science*, *340*(6138), 1314–1317. https://doi.org/10.1126/science.1233299

Cottrell, E., Kelley, K. A., Lanzirotti, A., & Fischer, R. A. (2009). High-precision determination of iron oxidation state in silicate glasses using XANES. *Chemical Geology*, *268*(3–4), 167–179. https://doi.org/10.1016/j.chemgeo.2009.08.008

Cottrell, E., Lanzirotti, A., Mysen, B., Birner, S., Kelley, K. A., Botcharnikov, R., et al. (2018). A Mössbauer-based XANES calibration for hydrous basalt glasses reveals radiation-induced oxidation of Fe. *American Mineralogist*, *103*(4), 489–501. https://doi.org/10.2138/am-2018-6268

Danyushevsky, L. V. (2001). The effect of small amounts of H2O on crystallisation of mid-ocean ridge and backarc basin magmas. *Journal of Volcanology and Geothermal Research*, *110*(3), 265–280. https://doi.org/10.1016/S0377-0273(01)00213-X

Danyushevsky, L. V., & Plechov, P. (2011). Petrolog3: Integrated software for modeling crystallization processes. *Geochemistry, Geophysics, Geosystems*, *12*(7), Q07021. https://doi.org/10.1029/2011GC003516

Davis, F. A., & Cottrell, E. (2021). Partitioning of Fe2O3 in peridotite partial melting experiments over a range of oxygen fugacities elucidates ferric iron systematics in mid-ocean ridge basalts and ferric iron content of the upper mantle. *Contributions to Mineralogy and Petrology*, *176*(9), 67. https://doi.org/10.1007/s00410-021-01823-3

Dick, H. J. B., Lin, J., & Schouten, H. (2003). An ultraslow-spreading class of ocean ridge. *Nature*, *426*(6965), 405–412. https://doi.org/10.1038/nature02128

Dixon, J. E., Stolper, E., & Delaney, J. R. (1988). Infrared spectroscopic measurements of CO2 and $H_2O$ in Juan de Fuca Ridge basaltic glasses. *Earth and Planetary Science Letters*, *90*(1), 87–104. https://doi.org/10.1016/0012-821X(88)90114-8

Font, L., Murton, B. J., Roberts, S., & Tindle, A. G. (2007). Variations in melt productivity and melting conditions along SWIR (70°E–49°E): Evidence from olivine-hosted and plagioclase-hosted melt inclusions. *Journal of Petrology*, *48*(8), 1471–1494. https://doi.org/10.1093/petrology/egm026

Gaetani, G. A. (2016). The behavior of $Fe^{3+}/\sum Fe$ during partial melting of spinel lherzolite. *Geochimica et Cosmochimica Acta*, *185*, 64–77. https://doi.org/10.1016/j.gca.2016.03.019

Gaetani, G. A., O'Leary, J. A., Shimizu, N., Bucholz, C. E., & Newville, M. (2012). Rapid reequilibration of $H_2O$ and oxygen fugacity in olivine-hosted melt inclusions. *Geology*, *40*(10), 915–918. https://doi.org/10.1130/G32992.1

Gardner, J. E., Jackson, B. A., Gonnermann, H., & Soule, S. A. (2016). Rapid ascent and emplacement of basaltic lava during the 2005–2006 eruption of the East Pacific Rise at ca. 9°51′N as inferred from CO2 contents. *Earth and Planetary Science Letters*, *453*, 152–160. https://doi.org/10.1016/j.epsl.2016.08.007

Georgeais, G., Koga, K. T., Moussallam, Y., & Rose-Koga, E. F. (2021). Magma decompression rate calculations with EMBER: A user-friendly software to model diffusion of $H_2O$, $CO_2$, and S in melt embayments. *Geochemistry, Geophysics, Geosystems*, *22*(7), e2020GC009542. https://doi.org/10.1029/2020GC009542

Ghiorso, M. S., Hirschmann, M. M., Reiners, P. W., & Kress, V. C. (2002). The pMELTS: A revision of MELTS for improved calculation of phase relations and major element partitioning related to partial melting of the mantle to 3 GPa. *Geochemistry, Geophysics, Geosystems*, *3*(5), 1–35. https://doi.org/10.1029/2001GC000217

Ghiorso, M. S., & Sack, R. O. (1995). Chemical mass transfer in magmatic processes IV. A revised and internally consistent thermodynamic model for the interpolation and extrapolation of liquid-solid equilibria in magmatic systems at elevated temperatures and pressures. *Contributions to Mineralogy and Petrology*, *119*(2), 197–212. https://doi.org/10.1007/BF00307281

Hamelin, B., & Allègre, C. J. (1985). Large-scale regional units in the depleted upper mantle revealed by an isotope study of the South-West Indian Ridge. *Nature*, *315*(6016), 196–199. https://doi.org/10.1038/315196a0

Hartley, M. E., Shorttle, O., Maclennan, J., Moussallam, Y., & Edmonds, M. (2017). Olivine-hosted melt inclusions as an archive of redox heterogeneity in magmatic systems. *Earth and Planetary Science Letters*, *479*, 192–205. https://doi.org/10.1016/j.epsl.2017.09.029

Hauri, E. H., Maclennan, J., McKenzie, D., Gronvold, K., Oskarsson, N., & Shimizu, N. (2018). $CO_2$ content beneath northern Iceland and the variability of mantle carbon. *Geology*, *46*(1), 55–58. https://doi.org/10.1130/G39413.1

Helo, C., Longpré, M.-A., Shimizu, N., Clague, D. A., & Stix, J. (2011). Explosive eruptions at mid-ocean ridges driven by $CO_2$-rich magmas. *Nature Geoscience*, *4*(4), 260–263. https://doi.org/10.1038/ngeo1104

Helz, R. T., Cottrell, E., Brounce, M. N., & Kelley, K. A. (2017). Olivine-melt relationships and syneruptive redox variations in the 1959 eruption of Kīlauea Volcano as revealed by XANES. *Journal of Volcanology and Geothermal Research*, *333–334*, 1–14. https://doi.org/10.1016/j.jvolgeores.2016.12.006

Herzberg, C., & Asimow, P. D. (2015). PRIMELT3 MEGA.XLSM software for primary magma calculation: Peridotite primary magma MgO contents from the liquidus to the solidus. *Geochemistry, Geophysics, Geosystems*, *16*(2), 563–578. https://doi.org/10.1002/2014GC005631

Hirschmann, M. M. (2018). Comparative deep Earth volatile cycles: The case for C recycling from exosphere/mantle fractionation of major ($H_2O$, C, N) volatiles and from $H_2O$/Ce, $CO_2$/Ba, and $CO_2$/Nb exosphere ratios. *Earth and Planetary Science Letters*, *502*, 262–273. https://doi.org/10.1016/j.epsl.2018.08.023

Iacono-Marziano, G., Morizet, Y., Le Trong, E., & Gaillard, F. (2012). New experimental data and semi-empirical parameterization of $H_2O$–$CO_2$ solubility in mafic melts. *Geochimica et Cosmochimica Acta*, *97*, 1–23. https://doi.org/10.1016/j.gca.2012.08.035

Janney, P. E., Le Roex, A. P., & Carlson, R. W. (2005). Hafnium isotope and trace element constraints on the nature of mantle heterogeneity beneath the central southwest Indian ridge (13°E to 47°E). *Journal of Petrology*, *46*(12), 2427–2464. https://doi.org/10.1093/petrology/egi060

Jarosewich, E., Nelen, J. a., & Norberg, J. A. (1980). Reference samples for electron microprobe analysis. *Geostandards Newsletter*, *4*(1), 43–47. https://doi.org/10.1111/j.1751-908X.1980.tb00273.x

Javoy, M., & Pineau, F. (1991). The volatiles record of a "popping" rock from the Mid-Atlantic Ridge at 14°N: Chemical and isotopic composition of gas trapped in the vesicles. *Earth and Planetary Science Letters*, *107*(3–4), 598–611. https://doi.org/10.1016/0012-821X(91)90104-P

Jenner, F. E., O'Neill, H. S. T. C., Arculus, R. J., & Mavrogenes, J. A. (2010). The magnetite crisis in the evolution of arc-related magmas and the initial concentration of Au, Ag and Cu. *Journal of Petrology*, *51*(12), 2445–2464. https://doi.org/10.1093/petrology/egq063

Jennings, E. S., & Holland, T. J. B. (2015). A simple thermodynamic model for melting of peridotite in the system NCFMASOCr. *Journal of Petrology*, *56*(5), 869–892. https://doi.org/10.1093/petrology/egv020

Jochum, K. P., Stoll, B., Herwig, K., Willbold, M., Hofmann, A. W., Amini, M., et al. (2006). MPI-DING reference glasses for in situ microanalysis: New reference values for element concentrations and isotope ratios. *Geochemistry, Geophysics, Geosystems*, *7*(2), Q02008. https://doi.org/10.1029/2005GC001060

Kamenetsky, V. S., Everard, J. L., Crawford, A. J., Varne, R., Eggins, S. M., & Lanyon, R. (2000). Enriched end-member of primitive MORB melts: Petrology and geochemistry of glasses from Macquarie Island (SW Pacific). *Journal of Petrology*, *41*(3), 411–430. https://doi.org/10.1093/petrology/41.3.411

Kress, V. C., & Carmichael, I. S. E. (1988). Stoichiometry of the iron oxidation reaction in silicate melts. *American Mineralogist*, *73*(11–12), 1267–1274.

Kress, V. C., & Carmichael, I. S. E. (1991). The compressibility of silicate liquids containing Fe2O3 and the effect of composition, temperature, oxygen fugacity and pressure on their redox states. *Contributions to Mineralogy and Petrology*, *108*(1–2), 82–92. https://doi.org/10.1007/BF00307328

Lange, R. A., & Carmichael, I. S. E. (1987). Densities of Na2O-K2O-CaO-MgO-FeO-Fe2O3-Al2O3-TiO2-SiO2 liquids: New measurements and derived partial molar properties. *Geochimica et Cosmochimica Acta*, *51*(11), 2931–2946. https://doi.org/10.1016/0016-7037(87)90368-1

Le Voyer, M., Hauri, E. H., Hauri, E. H., Cottrell, E., Kelley, K. A., Salters, V. J. M., et al. (2019). Carbon fluxes and primary magma $CO_2$ contents along the global mid-ocean ridge system. *Geochemistry, Geophysics, Geosystems*, *20*(3), 1387–1424. https://doi.org/10.1029/2018GC007630

Le Voyer, M., Kelley, K. A., Cottrell, E., & Hauri, E. H. (2017). Heterogeneity in mantle carbon content from $CO_2$-undersaturated basalts. *Nature Communications*, *8*(1), 14062. https://doi.org/10.1038/ncomms14062

Le Voyer, M., Rose-Koga, E. F., Shimizu, N., Grove, T. L., & Schiano, P. (2010). Two contrasting $H_2O$-rich components in primary melt inclusions from Mount Shasta. *Journal of Petrology*, *51*(7), 1571–1595. https://doi.org/10.1093/petrology/egq030

Mahoney, J., le Roex, A. P., Peng, Z., Fisher, R. L., & Natland, J. H. (1992). Southwestern limits of Indian Ocean Ridge mantle and the origin of low $^{206}Pb/^{204}Pb$ mid-ocean ridge basalt: Isotope systematics of the central Southwest Indian Ridge (17°–50°E). *Journal of Geophysical Research*, *97*(B13), 19771–19790. https://doi.org/10.1029/92JB01424

Marty, B., & Jambon, A. (1987). C3He in volatile fluxes from the solid Earth: Implications for carbon geodynamics. *Earth and Planetary Science Letters*, *83*(1–4), 16–26. https://doi.org/10.1016/0012-821X(87)90047-1

Mathez, E. A. (1976). Sulfur solubility and magmatic sulfides in submarine basalt glass. *Journal of Geophysical Research*, *81*(23), 4269–4276. https://doi.org/10.1029/JB081i023p04269

Matthews, S., Shorttle, O., Rudge, J. F., & Maclennan, J. (2017). Constraining mantle carbon: $CO_2$-trace element systematics in basalts and the roles of magma mixing and degassing. *Earth and Planetary Science Letters*, *480*, 1–14. https://doi.org/10.1016/j.epsl.2017.09.047

McKenzie, D., & O'Nions, R. K. (1991). Partial melt distributions from inversion of rare Earth element concentrations. *Journal of Petrology*, *32*(5), 1021–1091. https://doi.org/10.1093/petrology/32.5.1021

Métrich, N., Bertagnini, A., Landi, P., Rosi, M., & Belhadj, O. (2005). Triggering mechanism at the origin of paroxysms at Stromboli (Aeolian Archipelago, Italy): The 5 April 2003 eruption. *Geophysical Research Letters*, *32*(10), L10305. https://doi.org/10.1029/2004GL022257

Michael, P. J., & Graham, D. W. (2015). The behavior and concentration of $CO_2$ in the suboceanic mantle: Inferences from undegassed ocean ridge and ocean island basalts. *Lithos*, *236–237*, 338–351. https://doi.org/10.1016/j.lithos.2015.08.020

Mosbah, M., Metrich, N., & Massiot, P. (1991). PIGME fluorine determination using a nuclear microprobe with application to glass inclusions. *Nuclear Instruments and Methods in Physics Research Section B: Beam Interactions with Materials and Atoms*, *58*(2), 227–231. https://doi.org/10.1016/0168-583X(91)95592-2

Moussallam, Y. (2023a). SWIR XANES SPECTRA RAW.zip [Dataset]. Figshare. https://doi.org/10.6084/m9.figshare.24134970.v1

Moussallam, Y. (2023b). SWIR supplementary tables [Dataset]. Figshare. https://doi.org/10.6084/m9.figshare.24134976.v2
Moussallam, Y. (2023c). SWIR supplementary figures and text. [Dataset]. Figshare. https://doi.org/10.6084/m9.figshare.24134994.v1
Moussallam, Y., Edmonds, M., Scaillet, B., Peters, N., Gennaro, E., Sides, I., & Oppenheimer, C. (2016). The impact of degassing on the oxidation state of basaltic magmas: A case study of Kīlauea volcano. *Earth and Planetary Science Letters*, *450*, 317–325. https://doi.org/10.1016/j.epsl.2016.06.031
Moussallam, Y., Longpré, M.-A., McCammon, C., Gomez-Ulla, A., Rose-Koga, E. F., Scaillet, B., et al. (2019). Mantle plumes are oxidised. *Earth and Planetary Science Letters*, *527*, 115798. https://doi.org/10.1016/j.epsl.2019.115798
Moussallam, Y., Médard, E., Georgeais, G., Rose-Koga, E. F., Koga, K. T., Pelletier, B., et al. (2021). How to turn off a lava lake? A petrological investigation of the 2018 intra-caldera and submarine eruptions of Ambrym volcano. *Bulletin of Volcanology*, *83*(5), 36. https://doi.org/10.1007/s00445-021-01455-2
Moussallam, Y., Oppenheimer, C., Scaillet, B., Gaillard, F., Kyle, P., Peters, N., et al. (2014). Tracking the changing oxidation state of Erebus magmas, from mantle to surface, driven by magma ascent and degassing. *Earth and Planetary Science Letters*, *393*, 200–209. https://doi.org/10.1016/j.epsl.2014.02.055
Moussallam, Y., Rose-Koga, E. F., Koga, K. T., Médard, E., Bani, P., Devidal, J.-L., & Tari, D. (2019). Fast ascent rate during the 2017–2018 Plinian eruption of Ambae (Aoba) volcano: A petrological investigation. *Contributions to Mineralogy and Petrology*, *174*(11), 90. https://doi.org/10.1007/s00410-019-1625-z
Óladóttir, B. A., Sigmarsson, O., Larsen, G., & Thordarson, T. (2008). Katla volcano, Iceland: Magma composition, dynamics and eruption frequency as recorded by Holocene tephra layers. *Bulletin of Volcanology*, *70*(4), 475–493. https://doi.org/10.1007/s00445-007-0150-5
O'Neill, H. S. C. (2021). The thermodynamic controls on sulfide saturation in silicate melts with application to ocean floor basalts. In *Magma redox geochemistry* (pp. 177–213). American Geophysical Union (AGU). https://doi.org/10.1002/9781119473206.ch10
O'Neill, H. S. C., Berry, A. J., & Mallmann, G. (2018). The oxidation state of iron in Mid-Ocean Ridge Basaltic (MORB) glasses: Implications for their petrogenesis and oxygen fugacities. *Earth and Planetary Science Letters*, *504*, 152–162. https://doi.org/10.1016/j.epsl.2018.10.002
Pichavant, M., Carlo, I. D., Rotolo, S. G., Scaillet, B., Burgisser, A., Gall, N. L., & Martel, C. (2013). Generation of $CO_2$-rich melts during basalt magma ascent and degassing. *Contributions to Mineralogy and Petrology*, *166*(2), 545–561. https://doi.org/10.1007/s00410-013-0890-5
Rose-Koga, E. F., Koga, K. T., Schiano, P., Le Voyer, M., Shimizu, N., Whitehouse, M. J., & Clocchiatti, R. (2012). Mantle source heterogeneity for South Tyrrhenian magmas revealed by Pb isotopes and halogen contents of olivine-hosted melt inclusions. *Chemical Geology*, *334*, 266–279. https://doi.org/10.1016/j.chemgeo.2012.10.033
Rosenthal, A., Hauri, E. H., & Hirschmann, M. M. (2015). Experimental determination of C, F, and H partitioning between mantle minerals and carbonated basalt, $CO_2$/Ba and $CO_2$/Nb systematics of partial melting, and the $CO_2$ contents of basaltic source regions. *Earth and Planetary Science Letters*, *412*, 77–87. https://doi.org/10.1016/j.epsl.2014.11.044
Rudra, A., & Hirschmann, M. M. (2022). $Fe^{3+}$ partitioning between clinopyroxene and silicate melt at 1–2.5 GPa: Implications for $Fe^{3+}$ content of MORB and OIB source mantle. *Geochimica et Cosmochimica Acta*, *328*, 258–279. https://doi.org/10.1016/j.gca.2022.04.023
Saal, A., Hauri, E., Langmuir, C. H., & Perfit, M. (2002). Vapour undersaturation in primitive mid-ocean-ridge basalt and the volatile content of Earth's upper mantle. *Nature*, *419*(6906), 451–455. https://doi.org/10.1038/nature01073
Schiano, P., Monzier, M., Eissen, J.-P., Martin, H., & Koga, K. T. (2010). Simple mixing as the major control of the evolution of volcanic suites in the Ecuadorian Andes. *Contributions to Mineralogy and Petrology*, *160*(2), 297–312. https://doi.org/10.1007/s00410-009-0478-2
Shaw, A. M., Hauri, E. H., Fischer, T. P., Hilton, D. R., & Kelley, K. A. (2008). Hydrogen isotopes in Mariana arc melt inclusions: Implications for subduction dehydration and the deep-Earth water cycle. *Earth and Planetary Science Letters*, *275*(1), 138–145. https://doi.org/10.1016/j.epsl.2008.08.015
Shimizu, K., Saal, A. E., Hauri, E. H., Perfit, M. R., & Hékinian, R. (2019). Evaluating the roles of melt-rock interaction and partial degassing on the $CO_2$/Ba ratios of MORB: Implications for the $CO_2$ budget in the Earth's depleted upper mantle. *Geochimica et Cosmochimica Acta*, *260*, 29–48. https://doi.org/10.1016/j.gca.2019.06.013
Shimizu, K., Saal, A. E., Myers, C. E., Nagle, A. N., Hauri, E. H., Forsyth, D. W., et al. (2016). Two-component mantle melting-mixing model for the generation of mid-ocean ridge basalts: Implications for the volatile content of the Pacific upper mantle. *Geochimica et Cosmochimica Acta*, *176*, 44–80. https://doi.org/10.1016/j.gca.2015.10.033
Shishkina, T. A., Botcharnikov, R. E., Holtz, F., Almeev, R. R., & Portnyagin, M. V. (2010). Solubility of $H_2O$- and $CO_2$-bearing fluids in tholeiitic basalts at pressures up to 500 MPa. *Chemical Geology*, *277*(1–2), 115–125. https://doi.org/10.1016/j.chemgeo.2010.07.014
Shorttle, O., Moussallam, Y., Hartley, M. E., Maclennan, J., Edmonds, M., & Murton, B. J. (2015). Fe-XANES analyses of Reykjanes Ridge basalts: Implications for oceanic crust's role in the solid Earth oxygen cycle. *Earth and Planetary Science Letters*, *427*, 272–285. https://doi.org/10.1016/j.epsl.2015.07.017
Sorbadere, F., Laurenz, V., Frost, D. J., Wenz, M., Rosenthal, A., McCammon, C., & Rivard, C. (2018). The behaviour of ferric iron during partial melting of peridotite. *Geochimica et Cosmochimica Acta*, *239*, 235–254. https://doi.org/10.1016/j.gca.2018.07.019
Toplis, M. J. (2005). The thermodynamics of iron and magnesium partitioning between olivine and liquid: Criteria for assessing and predicting equilibrium in natural and experimental systems. *Contributions to Mineralogy and Petrology*, *149*(1), 22–39. https://doi.org/10.1007/s00410-004-0629-4
Treuil, M. (1975). *Utilisation des elements hygromagmatophiles pour la simplification de la modelisation quantitative des processus magmatiques*. Exemples de l'afar et de la dorsale medioatlantique.
Wallace, P., & Carmichael, I. S. E. (1992). Sulfur in basaltic magmas. *Geochimica et Cosmochimica Acta*, *56*(5), 1863–1874. https://doi.org/10.1016/0016-7037(92)90316-B
Wang, W., Kelley, K. A., Li, Z., Chu, F., Dong, Y., Chen, L., et al. (2021). Volatile element evidence of local MORB mantle heterogeneity beneath the southwest Indian ridge, 48°–51°E. *Geochemistry, Geophysics, Geosystems*, *22*(7), e2021GC009647. https://doi.org/10.1029/2021GC009647
Wanless, V. D., Behn, M. D., Shaw, A. M., & Plank, T. (2014). Variations in melting dynamics and mantle compositions along the Eastern volcanic zone of the Gakkel Ridge: Insights from olivine-hosted melt inclusions. *Contributions to Mineralogy and Petrology*, *167*(5), 1005. https://doi.org/10.1007/s00410-014-1005-7
Wanless, V. D., & Shaw, A. M. (2012). Lower crustal crystallization and melt evolution at mid-ocean ridges. *Nature Geoscience*, *5*(9), 651–655. https://doi.org/10.1038/ngeo1552
Workman, R. K., & Hart, S. R. (2005). Major and trace element composition of the depleted MORB mantle (DMM). *Earth and Planetary Science Letters*, *231*(1), 53–72. https://doi.org/10.1016/j.epsl.2004.12.005
Zhang, H. L., Cottrell, E., Solheid, P. A., Kelley, K. A., & Hirschmann, M. M. (2018). Determination of $Fe^{3+}$/ΣFe of XANES basaltic glass standards by Mössbauer spectroscopy and its application to the oxidation state of iron in MORB. *Chemical Geology*, *479*, 166–175. https://doi.org/10.1016/j.chemgeo.2018.01.006